Precision Engineering xxx (xxxx) xxx–xxx

Contents lists available at ScienceDirect

Precision Engineering

journal homepage: www.elsevier.com/locate/precision

Mechanical design and finite element analyses of surface bending mechanism for X-ray optics

Gong Xuepeng, Lu Qipeng*, Wang Yi, Song Yuan

State Key Laboratory of Applied Optics, Changchun Institute of Optics, Fine Mechanics and Physics, Chinese Academy of Sciences, Changchun 130033, China

ARTICLE INFO

Keywords:
Surface bending mechanism
X-ray optics
Synchrotron radiation
Mechanical design
Finite element analysis

ABSTRACT

A new surface diffraction beamline is designed at the Shanghai Synchrotron Radiation Facility (SSRF). The purpose is to provide a high-performance instrument for measurements of the surface interfaces of structures constructed using different materials for researchers from different countries. There are many technical difficulties associated with the construction of the beamline. One of them is the achievement of a high-focusing quality so as to reduce stray lights from substrates because of the small grazing incident angles. Two perpendicular focusing mirrors are adopted to focus the beam. In order to obtain an excellent light spot, the two mirrors are bent to obtain the expected curvature radii and surface errors. In this study, a new X-ray optics bending mechanism is designed for the mirrors, and its principle of operation is described. The mechanical state, the bending resolving power, and the suppression methods for surface errors are studied using finite element analyses. The mirror's minimum bending radius and bending resolving power are 1002 m and 24.2 m, respectively, and its suppression ability for surface error is better than 0.78 μrad. These characteristics are better than the predictions, and further improve the performance of the beamline.

1. Introduction

The synchrotron radiation light source is a revolutionary light source. The first synchrotron was built by Goward & Barnes in 1946, but the synchrotron light was not observable [1]. It was first observed by General Electric (GE) in 1947 as the phenomenon whereby an electron emits electromagnetic radiation when it rotates in a circle in a synchrotron, and was subsequently developed within a time period that spanned more than three generations. The first generation was a dual-purpose light source, "parasitically" running in synchrotrons. The second generation was a special light source whose purpose was to provide a powerful experimental tool for basic researchers in chemistry, biology, material science, and medicine. Owing to the promotion of the second generation light source to science and technology, major worldwide economic powers constructed the third generation light source in succession, achieving smaller beam divergence than the first and the second generation light sources that generally ranged between 5–12 nm·rad,thereby resulting in a higher spectral brilliancy [2]. Shanghai's Synchrotron Radiation Facility (SSRF) is equipped with a third generation light source, whereby dozens of beamlines have been established within it. High-brightness light beams from SSRF need to be deflected, collimated, monochromatized, and focused, by a series of high-performance optical devices.

The small beam divergence of the third generation light source results in a small grazing incidence angle (whereby for hard X-ray wavelengths, the grazing incidence angle is less than 5mrad), which gives rise to a long reflector length in the beam propagation direction, sometimes resulting in a length that exceeds 1m. With the current improvements in optical processing technologies, a highly accurate plane, or a highly accurate sagittal surface, can be manufactured on the surface of the mirror. However, it is difficult to manufacture a highly accurate cylindrical shape, or an elliptic cylinder shape whose radius is several kilometers along the meridional direction. Therefore, mechanical bending methods are usually adopted in the case of a large mirror to generate a deformation in the meridional direction to obtain a meridional shape. Through the use of the mechanical bending method, in addition to forming a highly accurate surface, the radius of the surface can be adjusted by controlling the bending force to adapt to different focal lengths and grazing incident angles. Dominating mechanical bending methods include three-point bending, four-point bending, two-arm bending, and flexible hinge bending [3–8]. Piezoelectric bending has emerged in recent years, which achieves a mirror bent by controlling numerous bimorphs between the mirror and its base in a segment-by-segment manner. This method is of high precision and high stability. It is usually applied to bend short-length mirrors [9].

In view of the characteristics of high-precision and high-economy of

* Corresponding author.
E-mail addresses: gongxuepeng120@foxmail.com (X. Gong), luqp@ciomp.ac.cn (Q. Lu).

https://doi.org/10.1016/j.precisioneng.2018.03.005
Received 22 December 2017; Received in revised form 5 March 2018; Accepted 16 March 2018

mechanical bending, researchers in synchrotron radiation facilities and beamline equipment suppliers all over the world have been studying in-depth different mechanical bending methods for large reflectors in order to develop superior performance mechanical bending equipment.

Depending on the surface diffraction beamline at SSRF, this study assesses a four-roller mechanical bending method using numerical simulations, and presents the development of a beamline bending equipment. This paper will elaborate the design process of the bending equipment, the mechanical state of the bending process, and the causes and suppression methods for surface errors, and will explain the relationship of the push-rod displacement, the mechanical state, the stress state, and the bending radius. The research outcomes presented herein are expected to provide detailed data and technical guidance for the future development of bending equipment with higher performance.

2. Design of the surface bending mechanism

The surface bending mechanism is designed primarily for the surface diffraction beamline at SSRF, and possesses general characteristics. The primary function of the beamline is the measurement of the interfaces of structures of all types of material surfaces. Relevant work includes research studies of low-dimensional membrane material interfaces and crystalline states, atomic structures and dynamics on solid surfaces, solid–liquid and liquid–liquid interfaces, structures of biofilms, and self-assembly of soft substances. The layout of the beamline is shown in Fig. 1. It makes full use of the low-divergence angle of undulator radiation, and adopts one monochromator and one focusing system to enhance photon flux and stability. A four-blade slit located at 21.5 m from the light source defines an acceptance angle of $0.08 \times 0.04\ \text{mrad}^2$ (H × V) for the optical elements downstream. A double-crystal monochromator located at 24 m from the light source defines the energy range and the energy resolution of the beamline. Two focusing mirrors located at 35 m and 37 m from the light source focus the beam in the vertical and horizontal directions, respectively. The two focusing mirrors are bent using bending equipment. This study aims to design the bending equipment of the focusing mirror that is located at 35m. The basic parameters of the focusing mirror are listed in Table 1, and the technical requirements of the bending equipment are listed in Table 2. Currently, the root-mean-square (RMS) slope error in the meridian direction can be controlled within 2–3 μrad using the mechanical bending method for a 1 m long mirror in synchrotron radiation beamlines. In some cases, fortunately, the RMS slope error can be close to 1 μrad. In this study, the requirement of the RMS slope error is 0.8 μrad.

2.1. Design principle

A four-roller bending scheme is implemented to design the bending device. There are two support rollers placed on the undersurface of the mirror, and two press rollers placed on the surface of the mirror. The distance between the support roller and the press roller is l_f. Each

Table 1
Basic parameters of the focusing mirror.

Item	Unit	Value
Dimensions of bending mirror	mm^3	1000′70′50
Effective area of bending mirror(L × W)	mm^2	840′40
Surface roughness	nm	≤0.3
Slope error in meridian direction	μrad	≤0.5
Base material		Monocrystal silicon

Table 2
Technical requirements of the bending device.

Item	Unit	Value
Minimum radius in meridian direction	m	≤2000
Root-mean-square (RMS) slope error of effective area of mirror after bending	mrad	≤0.8
Bending resolution	m	30(R: 2500–4500)

section of the mirror (spanning a distance l) will produce the same bending moment M when the press rollers exert the same forces F on the mirror. The surface of the mirror will generate a deformation with a radius R under the action of the bending moment M. The bending equation of the mirror is as follows,

$$M = \frac{EI}{R} \tag{1}$$

In Eq. (1), E is the modulus of elasticity of the mirror, I is the moment of inertia of the mirror, and R is the radius of the mirror after bending. Fig. 2 shows the principle of the four-roller bending scheme. After exerting a bending moment on the mirror, the deflection (deformation) of each section of the mirror is

$$y(M) = \frac{Mlx}{6EI}\left(1 - \frac{x^2}{l^2}\right) + \frac{Ml(l-x)}{6EI}\left(1 - \frac{(l-x)^2}{l^2}\right) \tag{2}$$

The largest deflection appears in the middle of the mirror. The slope of each section of the mirror is

$$\theta(M) = \frac{Ml}{6EI}\left(1 - \frac{3x^2}{l^2}\right) + \frac{Ml}{6EI}\left(-1 + \frac{3(l-x)^2}{l^2}\right) \tag{3}$$

2.2. Design of the bending component

The bending component is a key part used to determine the deformation of mirrors directly. It includes two support rollers, two press rollers, two rocker arms, a push rod, a support frame, and a water cooling pipe. Its structure is shown in Fig. 3. The motor rotates the screw rod, which makes the push block compress the spring whose deformation will produce a certain thrust. The thrust makes the push rod drive the two rocker arms that move in the opposite directions at the same time. The two rocker arms make the press rollers press the

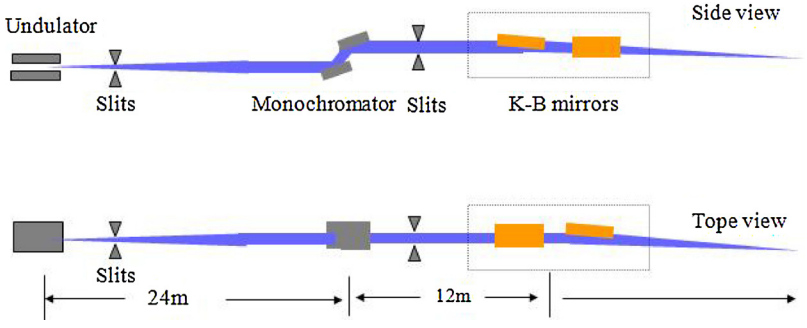

Fig. 1. Layout of the surface diffraction beamline. K-B is the abbreviation of Kirkpatrick-Baez.

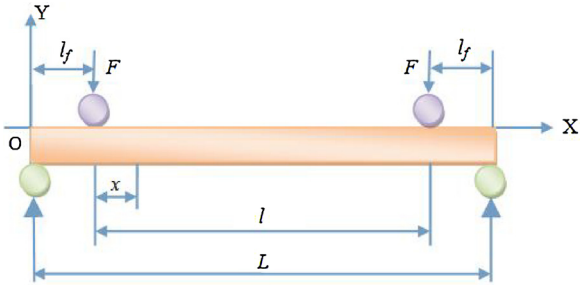

Fig. 2. Schematic depicting the principle of operation of the four-roller bending.

mirror. The pressure produced by the deformation of the compression spring makes the mirror generate a certain bending moment, and makes the mirror produce a bending deformation.

When a high-power synchrotron radiation irradiates the bending mirror, its surface and inner parts will generate a larger temperature gradient, which causes a thermal deformation in the mirror [10]. Therefore, the bending component is equipped with a water cooling structure. Two oxygen-free copper pieces are installed on both sides of the mirror by a fixing device, and a 1 mm indium membrane is used between the oxygen-free copper pieces and the mirror to improve the efficiency of heat conduction. A cooling water pipe is installed inside the copper pieces through which there is a circulation of 25 °C of cooling water to cool the mirror. In order to avoid the damage of the mirror when the high-power synchrotron radiation strikes the end of the mirror, a beam block is installed in front of the end of the mirror.

During the bending process, the most important concern is to control the radius of the mirror and its surface changes. The changes of the radius and surface shape will have an effect on the focusing ability of the mirrors. Both changes are directly related to the radius resolving power and the ability of the bending equipment to inhibit surface shape changes. The radius resolving power is related to the surface precision and the installation accuracy of the four rollers, the contact state between the rollers and the mirror, the displacement resolution of the push rod, and the stress state of the compression spring. The surface shape change is related to the mirror gravity and the performance of the gravity compensation mechanism. Therefore, in the following discourse, some numerical simulations will be performed to investigate these two aspects.

2.3. Overall structure of the surface bending mechanism

In synchrotron radiation beamline engineering, the X-ray surface bending mechanism is a key mechanism, and has some important roles. If a reflector is a sagittal cylindrical mirror, then after its bending using a bending mechanism, it will become a toroidal mirror with the focusing ability in the meridian and sagittal directions. If two perpendicular plane mirrors are bent by two bending mechanisms, they will become a Kirkpatrick-Baez (K-B) mirror system [10], and they can also focus the beam in the meridian and sagittal directions. In theory, a variety of surface shapes and radii of mirrors can be bent through a bending mechanism by controlling the bending moments on both ends of the mirror, and by changing the positions of the action points. The curvature equation is

$$\frac{\mathrm{EI}}{\rho(x)} = M(x) = M_1 + \frac{M_2 - M_1}{l}x \tag{4}$$

In Eq. (4), M_1 and M_2 are the bending moments on both ends of the mirror, and $\rho(x)$ is the radius of mirror at x point after bending. A cylindrical surface, a toroidal surface, an elliptical cylinder surface, or a parabolic surface, can be obtained by controlling M_1 and M_2 in theory.

The bending mechanism in this study is mainly used for forming a cylindrical mirror. In addition to the bending component and the alignment component described above, it also includes a vacuum chamber, a support structure, an isolated marble vibration table, three adjusting anchor bolts, a control system, and two ion pumps. The bending component is placed in the vacuum chamber, and its adjusting mechanism, circulating water cooling structure, and electric system, are realized by a vacuum–air interface. In order to guarantee the stability of the bending component after adjustment, it is necessary to control and minimize the vibration using some ISOLOC damping pads and a marble platform.

3. Finite element analysis of the surface bending mechanism

For the X-ray surface bending mechanism, its radius resolving power and its ability to minimize surface errors are two key performance indicators. To analyze the two capabilities in-depth, it is necessary to simulate the bending process using the finite element method. The stress state and bending state of the mirror; the relationship between the push rod's displacement, the deformation of the compression spring, and the bending radius; and the error inhibited state of the surface through the use of two-point, three-point, and four-point compensation methods are all analyzed in detail. Fig. 4 shows the finite element model of the bending component, including two press rollers, two support rollers, two rocker arms, a frame, and two push rod beams. The mirror is constructed using Si, and the materials of the other parts are 304 stainless steel.

3.1. Analysis of the stress state

In the case of four-roller bending, the bending of the mirror is equal to the bending of the beam. The mirror only generates an elastic deformation owing to the fact that the deformation of the mirror is very small during the bending process. Fig. 5 shows the simulation results for

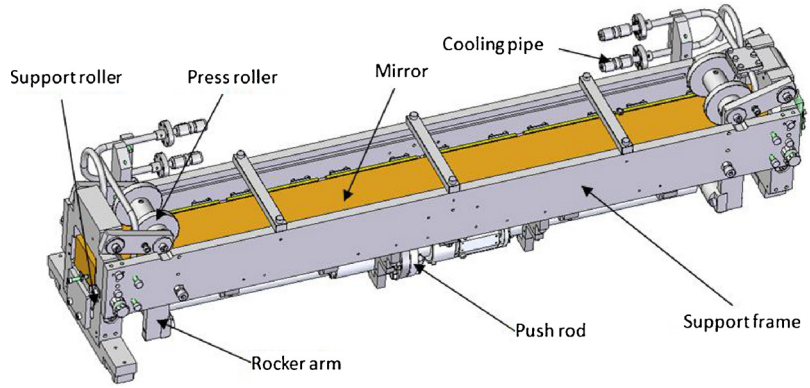

Fig. 3. Design scheme of the four-roller bending component.

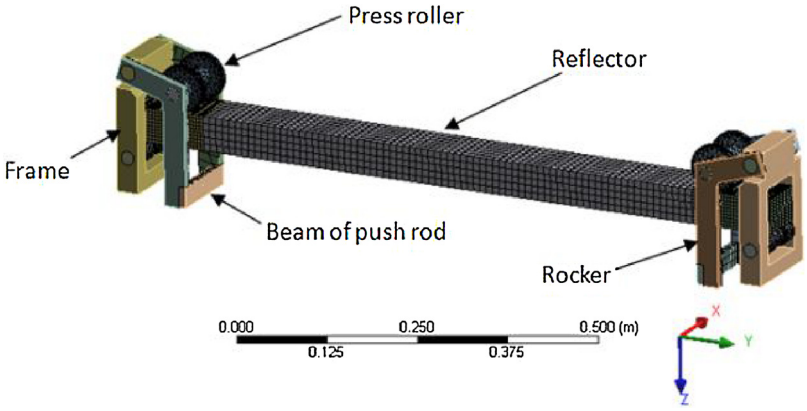

Fig. 4. Finite element model of the bending component.

the force during the bending of the mirror. The push block inside the push rod leads to a specific displacement based on the action of the step motor. This compresses the spring, and makes the spring generate a force that is transmitted to the rocker arms through the push rod, thereby acting on the mirror through the press rollers and the support rollers. Under the actions of the press and the support rollers, the mirror is bent. The press rollers are tangent to the surface of the mirror, and the force is always perpendicular to the contact interface between the press rollers and the mirror.

Fig. 6 shows the simulation results of normal stress distribution inside the mirror along the length direction for a push rod displacement of 120 μm. In the simulation, the compression spring is not introduced in order to simplify the model. In practice, in order to make the push rod move by 120 μm, the push block driven by the motor should move by a larger distance than the value listed, which is owing to the effect of the compression spring. In the actual testing process, it is necessary to formulate the relationship between the displacement of the push block and the bending radius of the mirror. These concepts will be analyzed in detail next. The bending deformation generated by the mirror is attributed to the normal stress of the mirror's cross-section. Considering the middle layer of the mirror as a boundary, the mirror can be divided into two parts, namely the upper and the lower parts. The resultant forces that the upper and the lower parts generate are equal, but the directions are opposite and not on the same line. Thus, the two resultant forces will form a force couple. The force couple will generate a bending moment on each cross-section. The bending moments on all the cross-sections will ensure that the mirror is bent. In Fig. 6, the maximum normal stress on the upper surface of the mirror is approximately -2.1×10^6 Pa (compressive stress), and the maximum normal stress on the lower surface of the mirror is approximately 2.1×10^6 Pa (tensile stress). For a certain cross-section, the changing rule of the normal stress requires that the compressive stress on the upper surface is the largest, and then gradually becomes smaller until it reaches a zero value in the middle layer. Stress then changes into tensile stress, and gradually becomes larger until it reaches its maximum value at the lower surface. This type of changing rule is embodied in the simulation results in a layered state. The tensile and compressive strength of quartz glass is used as a reference. Its tensile strength is approximately 48 MPa, and its compressive strength is approximately 785 MPa at 20 °C. In Fig. 6, the tensile stress and compressive stress of each cross-section are far less than the tensile and compressive strengths. In this case, the mirror can generate a specific bending deformation, while the failure will not occur. Fig. 7 shows the simulation results of the normal strain distribution inside the mirror along the length direction for a 120 μm displacement of the push rod. The normal strain and the normal stress obey Hooke's law in theory, and the coefficient of proportionality is the elastic modulus of the mirror. In Fig. 7, it is found that the changing rule of normal strain is the same as the changing rule of normal stress. Fig. 8 shows an equivalent deformation distribution of the mirror. The maximum deformation occurs in the middle cross-section of the mirror, and its value is approximately 82.6 μm. According to the numerical simulation results, it is found that the deformation of the mirror is induced mainly by the strain along the length direction, while the contributions of the strain along the direction that is perpendicular to the reflecting surface and the direction that is perpendicular to the mirror side are very small. Based on the maximum deformation of the mirror, it is easy to calculate the bending radius using the chord height formula. The bending radius can also be fitted by the deformations of all cross-sections.

3.2. Analysis of the bending radius resolving power

The bending radius resolving power is the most important index, for the surface bending mechanism. It has a considerable significance for online installation and focus of the light beam. Based on the above statements, the motor inside the push rod makes the push block compress the spring. In this compression process, the spring accumulates potential energy and generates a certain pressure. The pressure is transferred to the mirror through the push rod, the rocker arms, and the press rollers, and then forms two bending moments with the same values, but with opposite directions at both ends of the mirror under the action of the support rollers. When the bending moment formed by the spring pressure is zero (the spring does not generate a deformation), the bending radius of the mirror is infinite. When the spring generates a

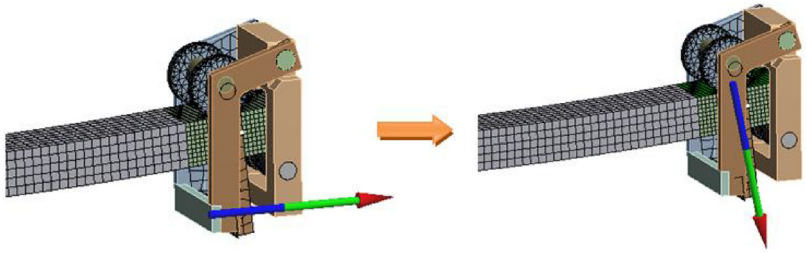

Fig. 5. Force simulation results of the mirror during the bending process.

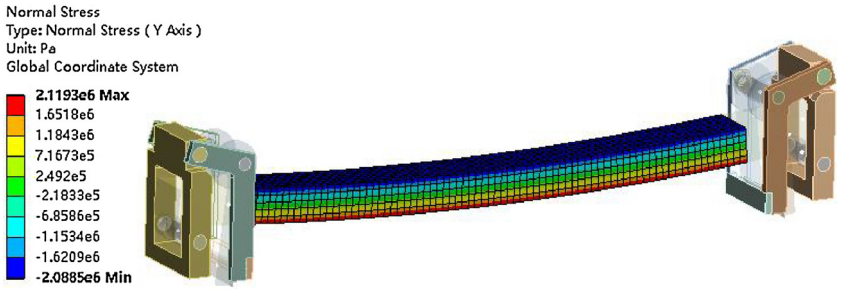

Fig. 6. Distribution of normal stress for a 120 μm displacement of the push rod.

small deformation (the bending moment is also very small), the bending radius of the mirror is very large and cannot meet the technical requirements. Only when the deformation of the spring (pressure) is within a certain range, the bending radius of the mirror can be set within the expected range. During the bending process, the push rod always contacts the rocker arms that connect the press rollers. In their turn, the press rollers always contact the surface of the mirror, thereby forcing the push rod to move by a corresponding distance to adapt to the deformation of the mirror. The displacement of the push rod is different from the displacement of the push block (the deformation of the spring). In the simulation, a displacement constraint is imposed on the push rod, thereby making the mirror deform. During the process, the reaction force of the push rod can be calculated, which corresponds to the pressure the spring creates. According to the stiffness coefficient $K = 9.6 \times 10^4$ N/m–1.05×10^5 N/m of the spring, and the force of the spring and Hooke's law, the deformation of the spring can be calculated. The deformation is the displacement of the push block, which is inside the push rod. The displacement is defined as a corrected displacement in this study. In an actual test, the relationship between the corrected displacement and the bending radius will be quantified.

Fig. 9 shows the deformation of the mirror under 20 μm step length of the push rod, and the relationship between the bending radius and the force of the push rod. The initial displacement of the push rod is 100 μm, and the corresponding bending radius is approximately 1700 m. In this condition, the force of the push rod is approximately 575N, and the corrected displacement of the push rod is 6 mm. After nine steps of bending, the radius is changed from R1700 m to R602m. If the step length of the push rod is 10 μm, 5 μm or 2 μm respectively, after nine steps of bending, the radius is changed from R1700 m to R942m, R1700 m to R1168 m or R1700 m to R1437 m respectively. The above observations show that in order to obtain a higher bending radius resolving power for the same initial bending radius, it is necessary to reduce the step length of the push rod, which means that the force increment of the push rod needs to be reduced. To achieve the goal, the reduction of the step length of the corrected displacement of the push rod (the displacement of the push block) is required. In Fig. 9(b), the bending radius decreases with the increase of the displacement of the push rod, but the relationship between the bending radius and the displacement of the push rod is not linear. The force of the push rod increases with the increase of the displacement of the push rod, and yields a linear relationship. According to the beam bending equation, the bending radius of the mirror is inversely proportional to the bending movements, and the bending moments are linearly related with the force of the push rod. Within the elastic deformation regime, the force and the displacement of the push rod are linearly related. Therefore, the bending radius and the displacement of the push rod are inversely proportional. When the step lengths of the push rod are the same, the variations of the bending radii are not the same. At the beginning of the deformation process, the variation of the bending radius is the largest. At the intermediate stage of the deformation, the variation of the bending radius becomes smaller. At the end of the deformation, the variation of the bending radius is the smallest.

Based on these statements, when conducting a bending resolving power test for a certain bending radius, we can establish the relationship of the bending radius, the bending radius after changing, and the displacement of the push block (the corrected displacement of the push rod). After this relationship is established, the increment of the corrected displacement can be determined, which is the displacement resolving power of the push block. A suitable stepper motor and some key components can be selected based on this value. In this study, the requirement of the bending resolving power is 30 m within the range of R2500m–R4500m. It is necessary to guarantee the bending resolving power at the maximum bending radius. In such a case, the bending resolving power of other bending radii can also meet the requirement.

The numerical relationship of the displacement of the push rod, the corrected displacement of the push rod, the force of the push rod, and the bending radius, can be established based on the results of Fig. 9. These outcomes are highly significant for predicting the performance of the surface bending mechanism, guiding the assembly, and correcting the deviation of the technical index. For example, when the bending radius is known, the force and the displacement of the push rod can be calculated. The two parameters are important for designing and selecting precision parts and quick-wear parts inside the push rod, and can provide a reference to optimize the structure of the push rod.

Fig. 10 shows the simulated results of the bending radius and the corrected displacement of the push rod. In Fig. 10, the variation of the bending radius is 30m. In this case, the corrected displacements of the push rod can be calculated for different bending radii. Correspondingly, the variations of the corrected displacements of the push rod can be calculated when the bending radius is increased 30m. The variation is

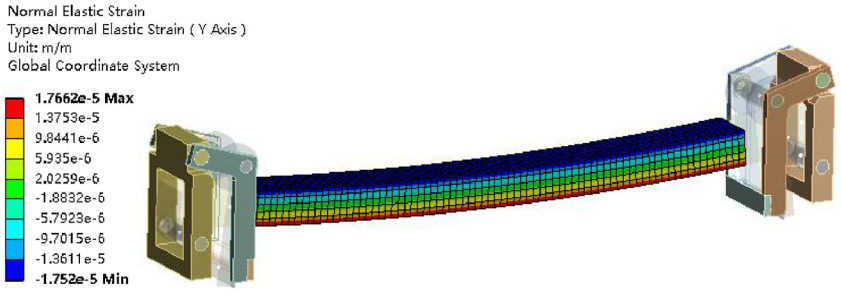

Fig. 7. Distribution of normal strain for a 120 μm displacement of the push rod.

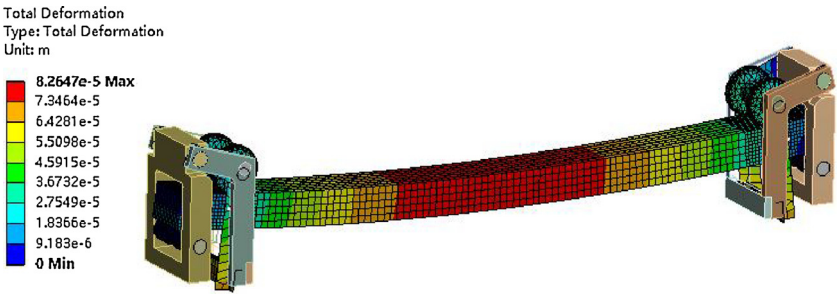

Fig. 8. Distribution of the equivalent deformation for a 120 μm displacement of the push rod.

the expected resolving power for the push rod. In Fig. 10, the corrected displacement of the push rod decreases with the increase of the bending radius, and the increment (absolute value) of the corrected displacement of the push rod also decreases. The variations of both of these variables are inversely proportional to the variation of the bending radius. When the bending radius changes from R1000m to R1030m, the increment of the corrected displacement is approximately 0.462 mm. When the bending radius changes from R2500m to R2530m, the increment of the corrected displacement is approximately 0.048 mm. When the bending radius changes from R4540m to R4570m, the increment of the corrected displacement is approximately 0.013 mm. For the same variation of the bending radius, and when the bending radius becomes larger, the push rod needs a higher resolving power for displacement, and it is necessary to put forward a higher requirement for the stepper motor, the ball screw, and the design of all the other key parts.

3.3. Analysis of surface error and its suppression methods

The surface error is a macroscopic measurement used to characterize the surface precision of optical elements, and indicates the divergence between an actual and an ideal surface shape. The surface error will affect the imaging quality and the resolving power of optical systems. In synchrotron radiation beamlines, the slope error of an optical element's surface is commonly used to express the surface error. The composite surface error of a bending mirror includes the machining error of the mirror, the errors induced by the structure of the bending mechanism, and the bending process, the error induced by the thermal deformation of the mirror irradiated by synchronous light, and the error induced by the gravity of the mirror. A large proportion of the surface error is the error induced by the gravity of the mirror [11–13]. Researchers have studied the error induced by the gravity of the mirror in-depth [14–16], but these studies have generally concentrated on the mathematical calculations and structural designs. Correspondingly, the studies on the fundamental causes of the surface error, theoretical analyses of the suppression method for the surface error, and on the change rule of the surface error, are fewer. Therefore, this study addressed the above issues using in-depth analyses, using the finite element method.

Fig. 11 shows the simulated results of the deformation and the normal stress along the length direction caused by gravity. The parameters of the mirror are shown in Table 1. The mirror is bent by the action of gravity, which is the reason that leads to the surface error. In Fig. 11, the surface of the mirror is in a compressive stress state, while the bottom surface of the mirror is in a tensile stress state. The two types of stresses have an equal absolute value, and the maximum value appears in the middle cross-section of the mirror. The normal stress decreases gradually from the middle of the mirror to the ends of the mirror. The normal stress distribution leads to the largest bending moment in the middle cross-section of the mirror, and makes the ends of the mirror generate the smallest bending moment. Ideally, when two identical forces are exerted on the ends of the mirror, the bending moments of each cross-section of the mirror become equal. In this case, the bending deformation of the mirror is considered as an expected deformation. Owing to the effects of gravity of the mirror, the bending moment on each cross-section increases slightly. Therefore, the increasing amplitude on each cross-section is different, and the increased amplitude on the middle cross-section is the largest, while the increased amplitudes on the ends are the smallest. The above reasons lead to the surface error between a real deformation and an expected deformation. In order to reduce the surface error induced by the gravity of the mirror, it is necessary to change the stress state of the mirror fundamentally. Ideally, the normal stress should be zero when the press rollers and the support rollers do not exert forces on the mirror, but it is difficult to realize this condition owing to the action of gravity. Therefore, other methods should be applied to reduce the normal stress inside the mirror

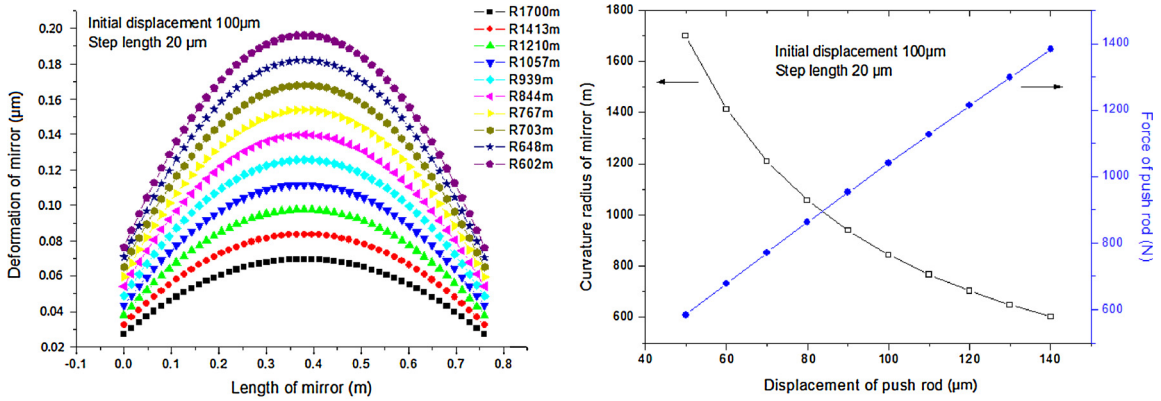

Fig. 9. Simulated results of deformations, and the relationships between the forces and the radii for 20 μm step length of the push rod.

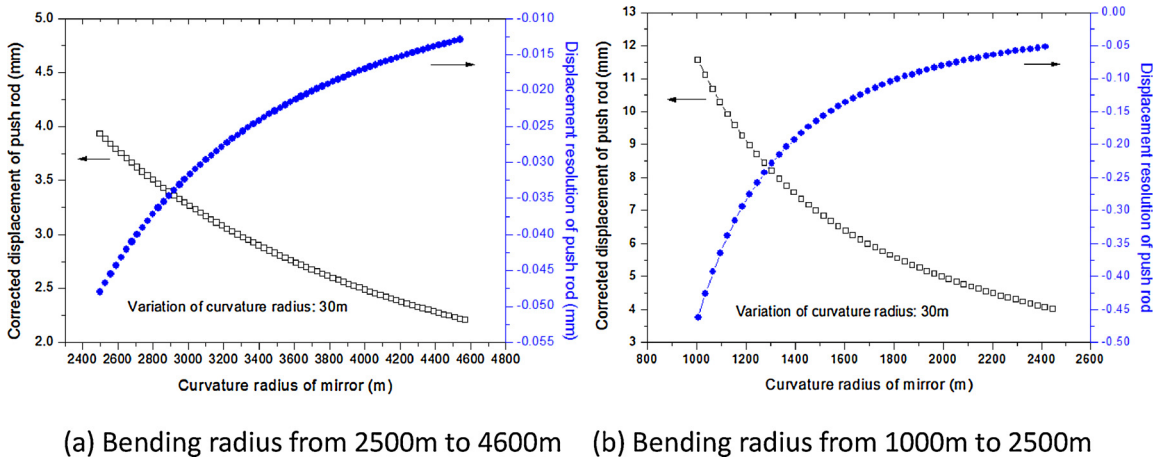

Fig. 10. Relationship between the corrected displacements of the push rod and the bending radii.

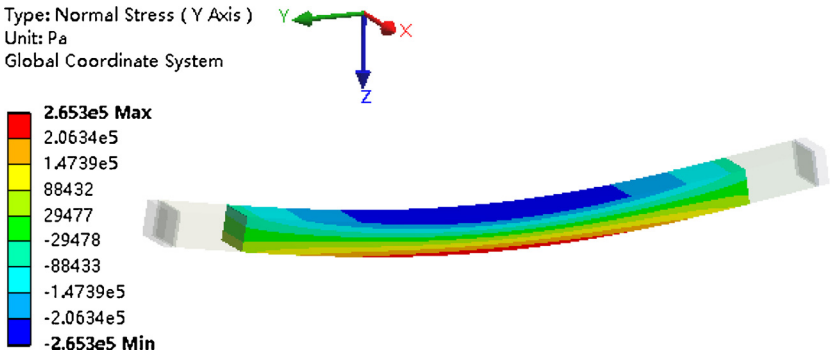

Fig. 11. Deformation and normal stress induced by the gravity of the mirror. The surface of the mirror is in a compressive stress state, while the bottom surface of the mirror is in a tensile stress state.

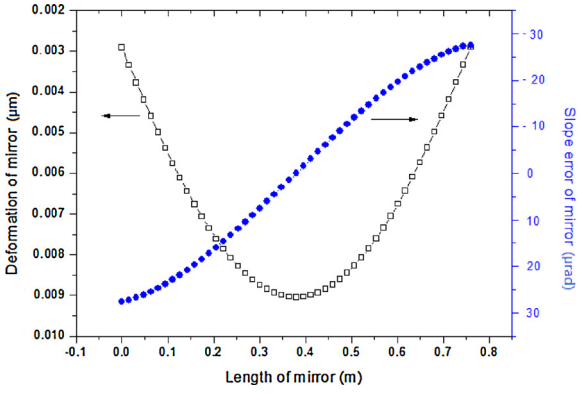

Fig. 12. Deformation and slope error induced by the gravity of the mirror. The RMS value of the slope errors induced by gravity is approximately equal to 10.8 μrad.

that is caused by gravity, thereby finally reducing the surface error to a reasonable level. Fig. 12 shows the simulated results of the deformation and the slope error induced by gravity. The maximum deformation is approximately 9.2 μm, the slope error on the middle cross-section is zero, and the slope errors on the ends of the mirror are the largest, with an absolute value of approximately 28 μrad. In synchrotron radiation beamlines, the RMS values of the slope errors of each cross-section are regarded as the surface errors. Based on calculations, the RMS value of the slope errors induced by gravity is approximately equal to 10.8 μrad.

The surface error has an adverse impact on image quality. It is necessary to apply additional methods to suppress it. The methods can be considered from two aspects. The first scheme involves the change of the nature of the mirror by using a material with high-strength and low-density (beryllium, silicon carbide) to reduce the ratio between the weight per unit length and the moment of inertia [17]. The second scheme involves the change of the structure of the bending mechanism to suppress the deformation caused by gravity. In this study, the second scheme has been adopted. Based on the above statements, if the normal stress of the mirror tends to zero, the surface error will be eliminated completely. If a uniform force is applied at the bottom of the mirror—which is equal to the gravity of the mirror and in a direction opposite to the direction of gravity—the deformation caused by gravity will be completely eliminated. However, this case is difficult to be realized in practice because of the complex structure of the bending mechanism. Some single forces applied at the bottom of the mirror can also suppress the deformation caused by gravity, and reduce the surface error to a certain extent. Based on above viewpoints, two-point, three-point, and four-point compensation methods, are analyzed in-depth herein.

For these compensation methods, the key point is to determine the distance between the support points, and the force on each support point. Considering the two-point compensation method as an example, the forces on the first and the second support points are F_{c1} andF_{c2}, respectively. The distance between the first support point and the first support roller is a, the distance between the second support point and the second support roller is b, and the distance between the first support point and the second point is d. The gravity per unit length is $q = G/l$, as shown in Fig. 13. Under the action of gravity and the forces of the two support points, the deformation of the mirror can be calculated by the following formulas [11].

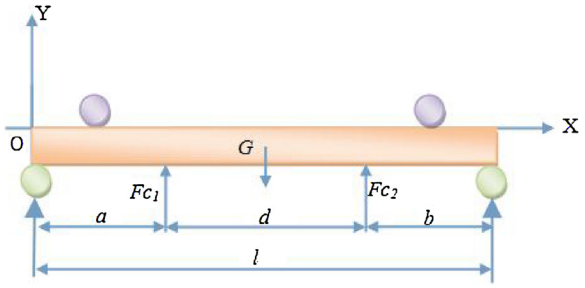

Fig. 13. Schematic diagram of the two-point compensation method.

$$y_a(G, Fc) = \frac{F_{c1}(d+b)x}{6lEI}(l^2 - x^2 - (d+b)^2) + \frac{F_{c2}bx}{6lEI}(l^2 - x^2 - b^2) - \frac{qx}{24EI}(l^3 - 2lx^2 + x^3) \quad 0 \le x \le a \tag{5}$$

$$y_d(G, Fc) = \frac{F_{c1}(d+b)}{6lEI}\left\{\frac{l}{(d+b)}(x-a)^3 + [l^2 - (d+b)^2]x - x^3\right\} + \frac{F_{c2}bx}{6lEI}(l^2 - x^2 - b^2) - \frac{qx}{24EI}(l^3 - 2lx^2 + x^3) \quad a \le x \le a + d \tag{6}$$

$$y_b(G, Fc) = \frac{F_{c1}(d+b)}{6lEI}\left\{\frac{l}{(d+b)}(x-a)^3 + [l^2 - (d+b)^2]x - x^3\right\} + \frac{F_{c2}b}{6lEI}\left[\frac{l}{b}(x-a-d)^3 + (l^2 - b^2)x - x^3\right] - \frac{qx}{24EI}(l^3 - 2lx^2 + x^3) \quad a + d \le x \le l \tag{7}$$

Considering the symmetrical deformation of the mirror and the symmetrical distribution of the support points, if $\alpha = \frac{Fc1}{ql} = \frac{Fc2}{ql}$, $\beta = \frac{d}{l}$, $a = b$, the slope error induced by the gravity of the mirror and the forces of the support points can be expressed as

$$\theta = \begin{cases} \frac{q}{6EI}\left[-x^3 - 3\left(\alpha - \frac{1}{2}\right)lx^2 + \frac{3}{4}\alpha l^3(1-\beta^2) - \frac{1}{4}l^3\right] & \left(x < \frac{l-d}{2}\right) \\ \frac{q}{6EI}\left[-x^3 + \frac{3}{2}lx^2 - 3\alpha l^2(1-\beta)\left(x - \frac{1}{2}l\right) - \frac{1}{4}l^3\right] & \left(\frac{l-d}{2} < x < \frac{l+d}{2}\right) \\ \frac{q}{6EI}\left[(l-x)^3 + 3\left(\alpha - \frac{1}{2}\right)(l-x)^2 l - \frac{3}{4}\alpha l^3(1-\beta^2) + \frac{1}{4}l^3\right] & \left(\frac{l+d}{2} < x < l\right) \end{cases} \tag{8}$$

For $x \in [0, l]$, and for different α and β, the average slope error is,

$$\theta_{RMS}(\alpha, \beta) = \sqrt{\frac{\int_0^l \theta^2(x)dx}{l}} \tag{9}$$

If α is a constant, β will change with changes in α, and will reach a minimum value. If β is a constant, α will change with changes in β, and will also reach a minimum value. By refining the values of α and β, we found that the slope error is close to a minimum when α = 0.389 and β = 0.390. When l = 1 m, we can calculate Fc = 31.09N and d = 390 mm. The calculation processes of the three-point compensation and the four-point compensation methods are similar to the two-point compensation method. These formulations are based on the mathematical formulation of bending theory. In practice, a concentrated force cannot completely concentrate at a point, and the spacing between the two support rollers is not equal to the length of the mirror but is slightly shorter. These items will result in a deviation between the actual condition and the calculation results. In this study, the distance between the two support points and the scope of forces on these support points are determined based on the above calculations, and the finite element model is then established to simulate the gravity compensation condition. For the two-point compensation method, the distance between points 1 and 2 is 390 mm. The separation width between the application points of the two forces on the bottom of the mirror is approximately 20 mm. Points 1 and 2 are symmetric based on the middle cross-section of the mirror. For the three-point compensation method, the distance between these points is 300 mm, and the three points are distributed symmetrically. For the four-point compensation method, the distance between these points is 218 mm, and the four points are symmetrically distributed.

Figs. 14–16 depict the gravity deformation simulation results of the two-point, three-point, and the four-point compensation methods, respectively. The purpose of gravity compensation is to keep the mirror surface in a plane state in the absence of bending moments, and reduce the normal stress inside the mirror as far as possible. In Fig. 14, the forces on the two support points are equal to 30.5N. Compared with the condition where only gravity acts on the mirror, the deformation of the mirror in Fig. 14 changes significantly, and resembles a wavy structure at the micro scale. In the area that contains these support points, the upper mirror surface is in a tensile stress state, and the bottom surface of the mirror is in a compressive stress state. Compared with the condition where only gravity acts on the mirror, the stress state also changes significantly. The variation of stress will lead to the change of the surface shape of the mirror, and will result in a change of the surface error. Only gravity acts on the mirror, and the upper surface of the mirror is in a compressive stress state, while the bottom of the mirror is in a tensile stress state. Correspondingly, the mirror surface generates a parabolic deformation. The deformation on both ends of the mirror is very steep and it leads to large surface errors on both ends of the mirror. The deformation on the middle part of the mirror is very small, and leads to small surface errors. When the mirror is supported by two points, the gradient of the deformation on both the ends of the mirror decreases, and the deformation at the support points and at the middle parts of the mirror also become smaller. In accordance to this condition, the surface error on each cross-section of the mirror is reduced. The three-point and the four-point compensation methods lead to progressively smaller deformations for each cross-section of the mirror, and avoid generation of large gradient deformations, thereby leading to further reductions in the surface error. In Fig. 15, the forces on the three

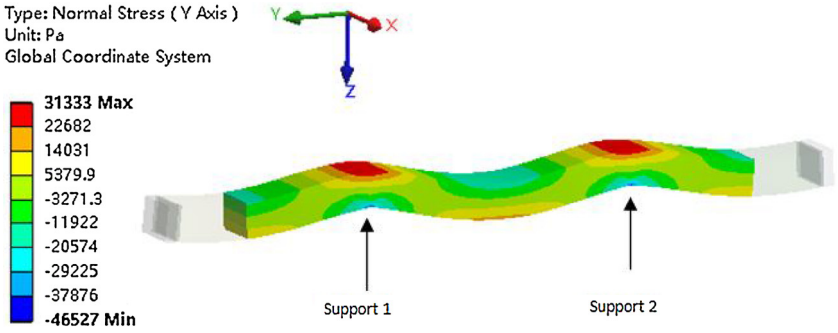

Fig. 14. Simulation results of the two-point compensation method. The forces on the two support points are equal to 30.5N.

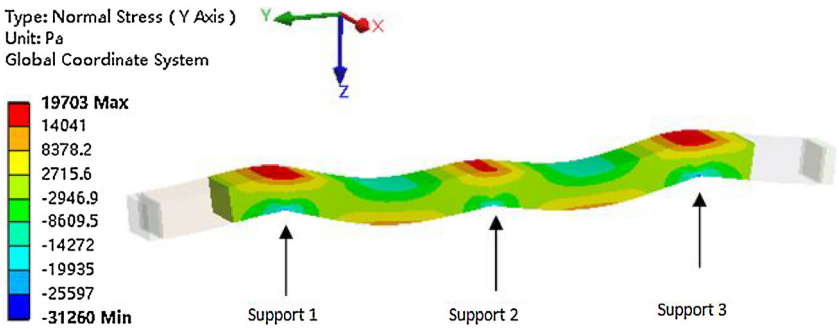

Fig. 15. Simulation results of the three-point compensation method. The forces on the three support points are equal to 23.2N.

support points are equal to 23.2N. In Fig. 16, the forces on support points 1 and 4 are 17.35N. The forces on support points 2 and 3 are 17.25N. In Fig. 11, only gravity acts on the mirror, and the maximum compressive stress is -2.653×10^5 Pa, and the maximum tensile stress is 2.653×10^5 Pa. In Fig. 14, for the two-point compensation, the maximum compressive stress is −45.627 kPa, and the maximum tensile stress is 31.333 kPa. In Fig. 15, for the three-point compensation, the maximum compressive stress is −31.260 kPa, and the maximum tensile stress is 19.703 kPa. In Fig. 16, for the four-point compensation, the maximum compressive stress is −19.001 kPa, and the maximum tensile stress is 10.359 kPa. From these data, it can be found that only gravity acts on the mirror, and the normal stress inside the mirror is the largest. In the two-point compensation condition, the normal stress is smaller compared to the above condition. Correspondingly, in the three-point compensation condition, the normal stress is smaller compared to the two conditions described above, and in the four-point compensation condition, the normal stress is the smallest. These phenomena show that the span of the normal stress inside the mirror reduces, the gradient of the deformation reduces, and the surface error eventually reduces through the use of these compensation methods.

The stress states of the two-point, three-point, and the four-point compensation methods are analyzed next. In Fig. 17(a), when the forces of support points 1 and 2 are equal to 30N, the two support points cannot completely overcome the gravity deformation. Under the actions of gravity and these support points, the main deformation of the mirror is the deformation caused by gravity, and the range of this deformation is approximately 0.06 μm–0.17 μm. In this case, the slope error of the mirror surface is shown as a red curve in Fig. 17(b), and the RMS value of the slope error is approximately 0.417 μrad, which is far less than the RMS value of the slope error subject to the condition that only gravity acts on the mirror. When the forces of the two support points are equal to 31N, the influence of the support forces on the deformation of the mirror is greater than the influence of gravity, and the range of the elicited deformation is approximately −0.03 μm–0.04 μm. In this case, the slope error of the mirror surface is shown as a black curve in Fig. 17(b), the RMS value of the slope error is approximately 0.615 μrad. Although the above two stress states exhibit good suppression effects on the slope error of the mirror, they still do not reach the optimized state achieved in the case of the two-point compensation method. The variation of the deformation of the mirror under the condition at which the forces of the two support points are equal to 30.6N is shown as a deep blue curve in Fig. 17(a), the elicited range of the deformation is approximately −0.08 μm–0 μm, and the RMS value of the slope error is approximately 0.408 μrad. The variation of the deformation of the mirror under the condition at which the forces of the two support points are 30.4N is shown as a light blue curve in Fig. 17(a), the elicited range of deformation is approximately equal to −0.03 μm–0.04 μm, and the RMS value of the slope error is approximately 0.393 μrad. It can be found that only the forces of the two support points are less than 30.6N (and thus higher than 30.4N), while the deformation curve of the mirror can lie between the deep blue curve and the light blue curve in Fig. 17(a), and further reduces the slope error of the mirror. When the forces of the two support points are 30.5N, the deformation of the mirror is plotted as the green curve in Fig. 17(a), and is uniform compared to other situations. At this time, the slope error of the mirror is shown as a green curve in Fig. 17(b). The peak and trough values are basically the same. There are no obvious high points and low points. The RMS value of the slope error is approximately equal to 0.377 μrad. In regard to the two-point compensation method, the condition whereby the forces of the two support points are equal to 30.5N is close to the optimized state in terms of the slope error suppression. If the search continues for a more accurate force setting in the vicinity of 30.5N, the elicited state can continue to approach the theoretically optimized state. In practice, there is no meaning in pursuing this search because a more accurate pressure sensor and a more rigorous installation and debugging process will be needed, yet it becomes more difficult to further reduce the slope error.

In order to further reduce the slope error, the number of the support points should be increased. Different mirror deformations and slope errors are simulated in Fig. 18 using the three-point compensation method. Similar to the two-point compensation method, the forces of the support points for the three-point compensation method need to be

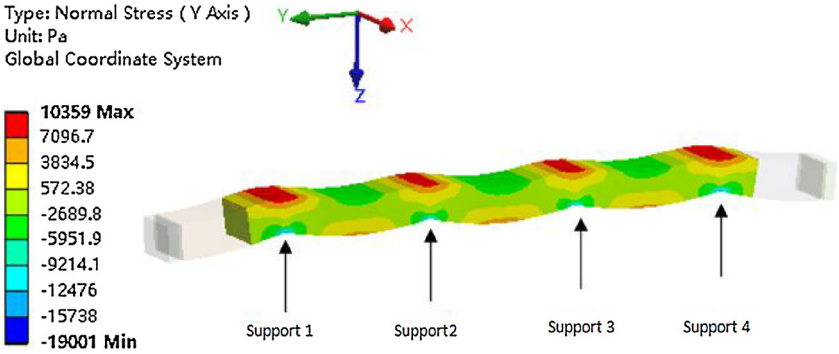

Fig. 16. Simulation results of the four-point compensation method. The forces on support points 1 and 4 are 17.35N. The forces on support points 2 and 3 are 17.25N.

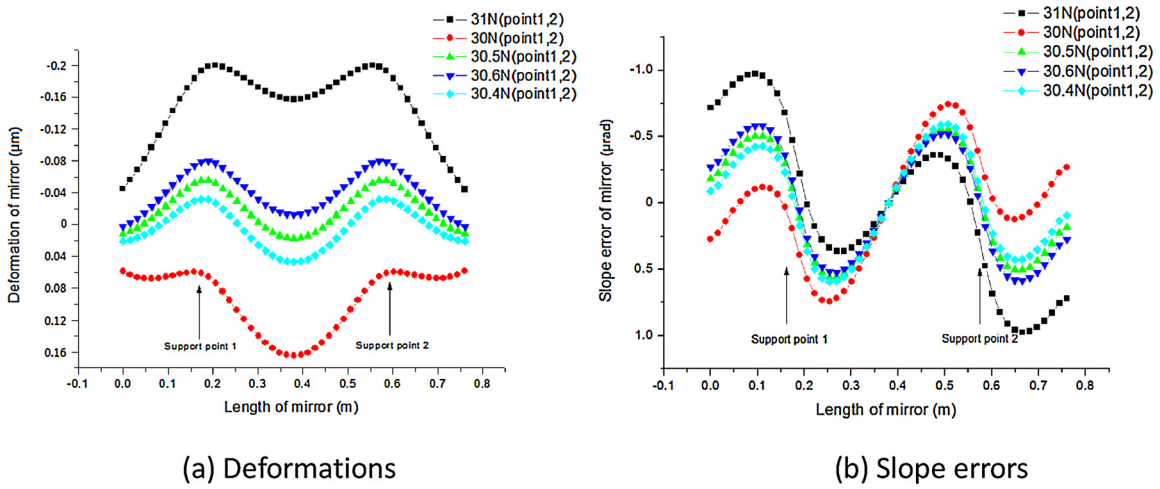

Fig. 17. Simulation results of the two-point compensation method. It has the best effect when the forces of the two support points are 30.5N.

controlled to suppress the slope error of the mirror. Because the mirror and the three support points are symmetric, the forces of support points 1 and 3 should be same. The force of support point 2 can be different from the other two. In Fig. 18(a), when the forces of the three support points are 23.5N and 23.2N, respectively, the deformation of the mirror is not homogeneous. In Fig. 18(b), the slope errors of the two conditions are not homogeneous either. The differences between the peak and trough values are larger. The RMS values of the slope errors of the two conditions are 0.287 μrad and 0.216 μrad, respectively. When the forces of support points 1 and 3 are 23N, the force of support point 2 is 23.6N, and the RMS value of the slope error is 0.209 μrad. When the forces of support points 1 and 3 are 22.8N, the force of support point 2 is 23.8N, and the RMS value of the slope error is 0.207 μrad. When the forces of support points 1 and 3 are 22.9N, the force of support point 2 is 23.7N, and the RMS value of the slope error is 0.205 μrad. The deformation curves and slope error curves of these three conditions are very close. This suggests that in an actual installation and debugging process, if the three-point compensation method is adopted, only the forces of the three support points are controlled in the range of these three conditions, and the slope error of the mirror can be adequately suppressed.

Fig. 19 shows the simulation results of the deformation and slope errors for the four-point compensation method. When the forces of the four support points are 17N and 17.5N respectively, the RMS values of the slope errors are 0.294 μrad and 0.251 μrad, respectively. When the forces of the four support points are 17.3N, the RMS value of the slope error is 0.09 μrad. When the forces of support points 1 and 4 are 17.35N, the forces of support points 2 and 3 are 17.25N, and the RMS of the slope error is 0.088 μrad. When the forces of support points 1 and 4 are 17.35N, the forces of support points 2 and 3 are 17.26N, and the RMS value of the slope error is 0.087 μrad.

Fig. 20 shows the comparative results of the two-point, three-point, and the four-point compensation methods. The slope error curves of the three methods present some cyclical fluctuation states. The absolute peak and trough values, and the cycle of the curve of the two-point compensation method are the largest, followed by the three-point and the four-point compensation methods. It can be found that in a reasonable installation and debugging process, the four-point compensation method elicits the best slope error suppression effects, but increases the complexity of the bending mechanism. Therefore, for the bending mechanism, if the two-point compensation method can achieve adequate suppression of the slope error, it would be desirable to adopt it. However, in the case where the two-point method elicits inadequate outcomes, the three-point and the four-point compensation methods will be considered.

4. Performance testing of the bending mechanism

The key indicators of the surface bending mechanism include the minimum bending radius in the meridian direction, the surface error in the meridian direction, and the bending resolving power. The previous

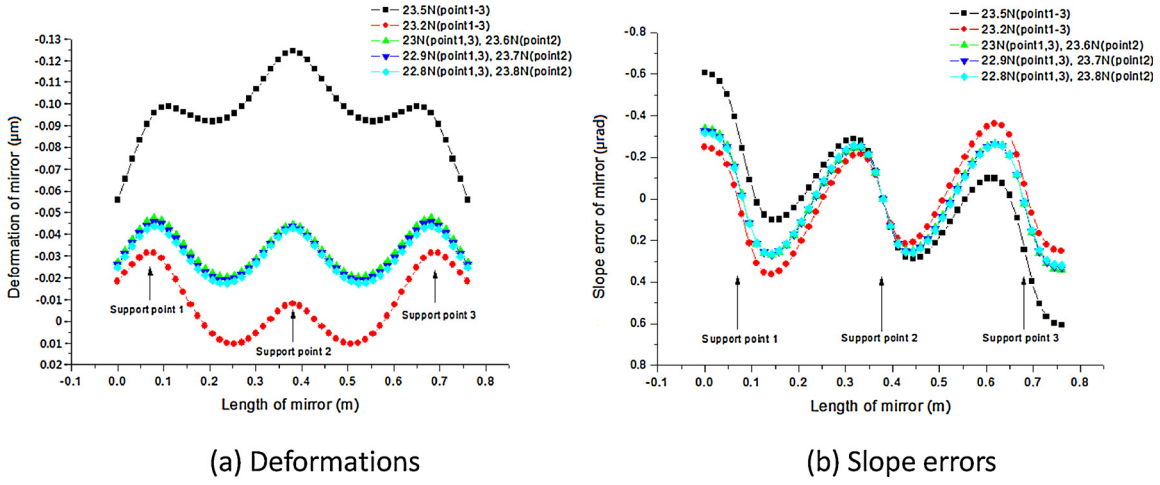

Fig. 18. Simulation results of the three-point compensation method. It has the best effect when the forces of support points 1 and 3 are 22.9N, and the force of support point 2 is 23.7N.

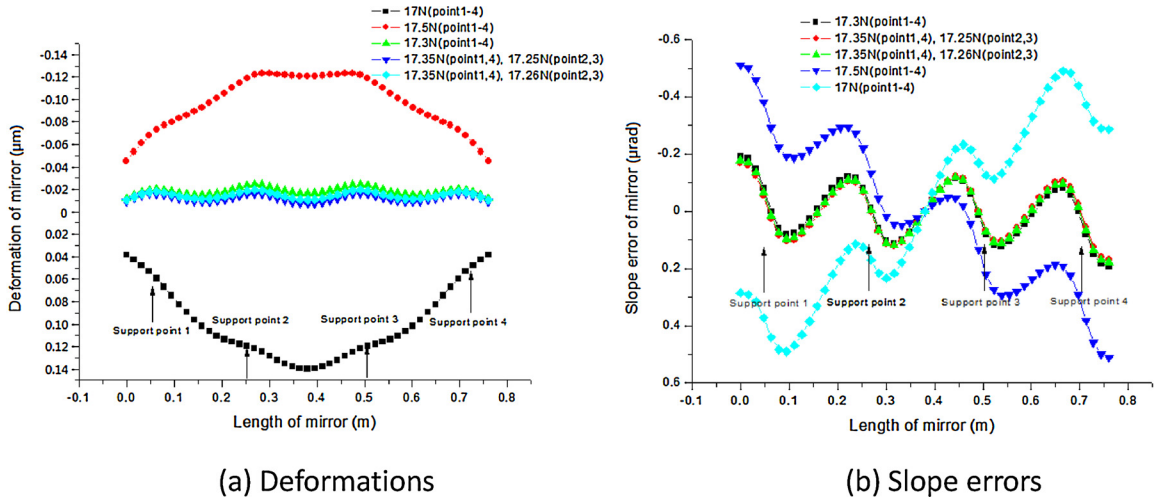

Fig. 19. Simulation results of the four-point compensation method. It has the best effect when the forces of support points 1 and 4 are 17.35N, the forces of support points 2 and 3 are 17.26N.

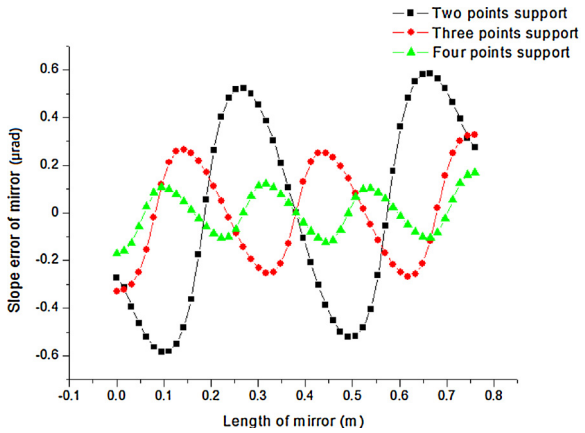

Fig. 20. Comparison results of the two-point, three-point, and the four-point compensation methods. The four-point compensation method elicits the best slope error suppression effects, but increases the complexity of the bending mechanism.

sections discussed the analyses, the bending resolving power, and the suppression of the surface error. This section will test these key indicators by using some related instruments. Fig. 21 shows a photograph of the bending mechanism. A long trace profiler (LTP-1200) is used to test the radius and the slope distribution of the mirror. Its measuring precision is 0.2 μrad and its resolution is 0.1 μrad. Its largest measuring length is 1200 mm.

The bending mechanism that is equipped with a mirror is installed on the LTP-1200. The optical system of the LTP-1200 is adjusted to suit the measurement of the bending radius. The step motor inside the push rod is rotated to force the push block inside the rod to move by the maximum travel distance. At this time, the press rollers and the support rollers generate the largest bending moment. After testing, the bending radius is 1002m, which is better than the requirement. According to the requirement of this beamline, the limits of the push block are adjusted to make the minimum bending radius smaller than 2000m. After the adjustment, the minimum bending radius is approximately equal to 1906m.

Before measuring the surface error, the initial state of the mirror must be not affected by external forces. When the push block is forced to move by 2 mm and 6 mm, respectively, the surface errors of the two bending states can be measured. Each bending state is measured five times, and the RMS value of the five bending state values is considered as the surface error. The measured results are shown in Fig. 22. The surface error in the first state is approximately 0.78 μrad, and the surface error in the second state is approximately 0.62 μrad. Thus, they are both in compliance with the design requirements.

Fig. 21. Photograph showing the surface bending mechanism on the LTP-1200.

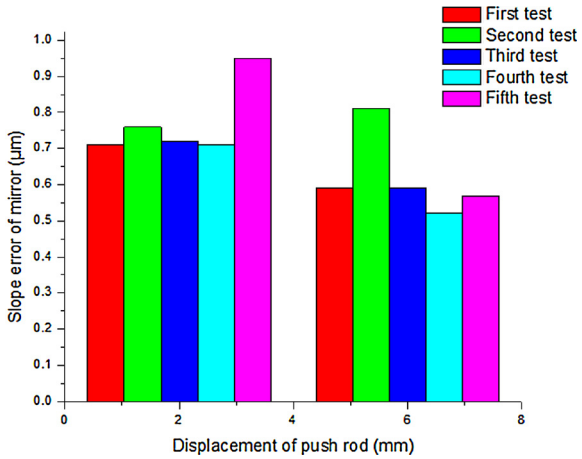

Fig. 22. Testing results of surface error. It is approximately 0.78 μrad in the first state, and is approximately 0.62 μrad in the second state.

Fig. 23(a) shows the test results of the bending resolving power for bending radii that are smaller than 2500m. The push block is then forced to move by 4 mm, 5 mm, and 6 mm, respectively, and subsequently in 50 μm increments in a continuous manner for five times at each point. The change of the bending radius is then measured using the LTP-1200. The mean of the measured results is then estimated as the bending resolving power. When the displacement of the push block is 4 mm, the bending radius is approximately 2445m, and the change of the bending radius is approximately 18m, 23m, 30m, 17m, and 33m, respectively, at each of the five 50 μm step length increments, with the mean value being approximately equal to 24.2m. When the displacement of the push block is 5 mm, the bending radius is approximately equal to1989m, and the mean of the change of the bending radius is approximately 15.8m. When the displacement of the push block is 6 mm, the bending radius is approximately 1692m, and the mean change of the bending radius is approximately 12.6m. Fig. 23(b) shows the test results of the bending resolving power when the bending radius is larger than 2500m. The push block is driven to move by 1.7 mm, 2.8 mm, and 3.2 mm, respectively. At each point, the push block is then driven to move in 10 μm steps in a continuous manner for five times. The test results show that the mean change of the bending radius is approximately equal to17.75 m for R5944m, 5.75 m for R3473m, and 5.5 m for R3091m. These test results meet the design requirements.

The experimental parameters in the bending resolving power testing process are input to the finite element model, and the bending process is simulated. The simulated and the experimental results for the bending radius, which is smaller than 2500 m, are shown in Fig. 24. This shows that the change trend of the experimental results and the simulated results are basically identical.

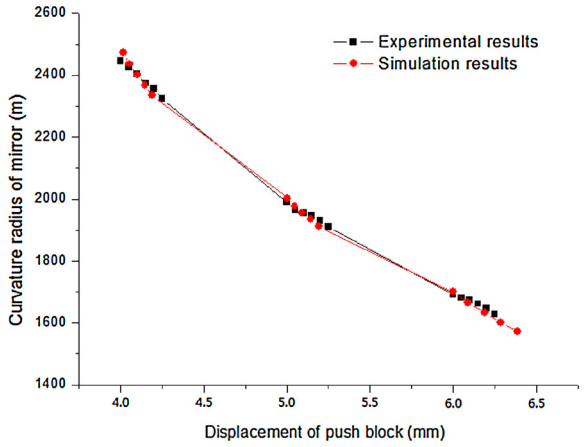

Fig. 24. Comparison of experimental and simulated results in the condition of bending radius smaller than 2500m. The change of the bending radius is measured using the LTP-1200. The change trend of the experimental results and the simulated results are basically identical.

5. Conclusions

Based on the surface diffraction beamline at SSRF, the design and numerical simulations of a high-performance X-ray optics bending mechanism were completed. In view of the high-precision and high-economic efficiency characteristics of the mechanical bending method, the four-roller bending scheme was adopted to complete the overall design of the bending mechanism. The structure and the movement of the four-roller bending component were stated and analyzed. The mechanical state, the bending resolving power, and the suppression method of the surface error in the bending process were analyzed in-depth. In the conducted analyses, it was pointed out that the normal stress inside the mirror was the major reason that led to the induction of the bending of the mirror, and the strain along the length direction contributed significantly to the bending deformation of the mirror. The bending resolving power was related to the displacement of the push rod, the driving force, and the spring stiffness. Using the same displacement increment conditions, the change of the radius for the largest bending radius was the most sensitive during a specific range of bending radii. Changes in the stress state of the mirror can improve the surface shape during the bending process in a reasonable manner.

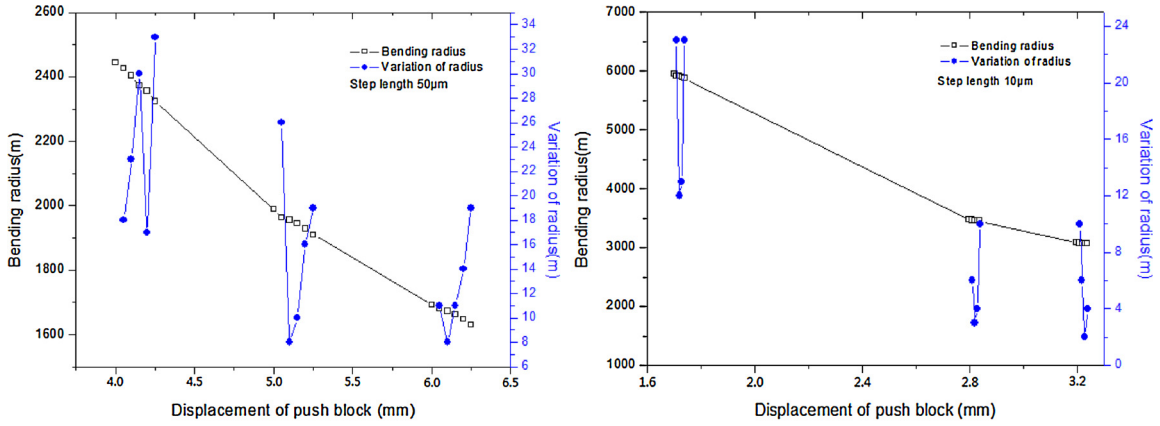

(a) Bending radius smaller than 2500m (b) Bending radius larger than 2500m

Fig. 23. Experimental results of the bending resolving power. It is less than 30 m from bending radius 6000 m to 1500 m.

Additionally, a supporting device can be installed at the bottom surface of the mirror to change the deformation, thereby suppressing the surface error. Owing to the structural complexity of the multipoint compensation method, it is better to adopt the two-point compensation method to suppress the surface error under the premise that the technical requirements can be met. The mechanical performances were tested, and led to a minimum bending radius of approximately 1002 m, a surface error of approximately 0.78 μrad, and a bending resolving power of approximately 24.2 m.

Acknowledgments

This work was funded by the National Nature Science Foundation of China (No. 61404139), the National Science and Technology Major Project (No. 2012ZX02702001-005), the Independent fund of State Key Laboratory of Applied Optics (Y5743FQ158), the Key Science and Technology Achievements Transformation Projects of Jilin Province (20150307039GX), and the National Major Scientific Project of China (SS–06).

The authors thank the staff of the surface diffraction beamline at the Shanghai Synchrotron Radiation Facility.

References

[1] Goward FK, Barnes DE. Letters to the editors-experimental 8 Mev. synchrotron for electron acceleration. Nature 1946;4012:413.
[2] Andreas KF. Third-generation synchrotron radiation X-ray optics. Facility Struct 1996;4(2):121–5.
[3] Kamachi N, Endo K, Ohasi H, et al. Characteristics of mechanically-bent-shaped mirror: experimental study on stability using LTP II. 8th International conference on synchrotron radiation instrumentation. 2003. p. 8.
[4] Padmore HA, Howells MR, Irick S, Senner T, Sandler R, Koo YM. Some new schemes for producing high-accuracy elliptical x-ray mirrors by elastic bending. SPIE 1996;2856:145–1155.
[5] Lienert Ulrich, Hartlaub Siegid, Freund Andreas K. Experimental shape optimization of bent crystals. SPIE 2018;3152:120–4.
[6] Beynon TD, Kirk I, Mathews TR. Gabor zone plate with binary transmittance values. Opt Lett 2016;1992(17):544–6.
[7] Zettl B, Szyszkowski W, Zhang WJ. Accurate low DOF modeling of a planar compliant mechanism with flexure hinges: the equivalent beam methodology. Precis Eng 2005;29:237–45.
[8] Kamachi N, Endo K, Ohasi H, Ishikawa T. Characteristics of mechanically-bent-shaped mirror. Experimental study on stability using LTP II. 8th International Conference on Synchrotron Radiation Instrumentation (SRI 2003). 2003.
[9] Freund AK. X-ray optics at the European synchrotron radiation facility. SPIE 1995;2515:445–57.
[10] Gong Xuepeng, Lu Qipeng, Song Yuan. Mechanical design and performance evaluation of KB mirror system for the ARPES beamline at SSRF. Precis Eng 2016;46:166–76.
[11] Howells Malcolm R, Lunt David L. Design considerations for adjustable-curvature, high-power, x-ray mirrors based on elastic bending. Opt Eng 2016;32(8):1981–9.
[12] Ice G.E. On controlling gravitational distortions in long synchrotron x-ray mirrors. United States, N. p., 1996. Web.
[13] Nistea IT, Alcock SG, Kristiansen P, Young A. Long, elliptically bent, active X-ray mirrors with slope errors < 200 nrad. J Synchrotron Radiat 2017;24:615–21.
[14] Fu Yuan, Zhu Wanqian, Xue Song. The development of SSRF beamline mirror manipulator systems. Nucl Techn 2010;33(10):725–9.
[15] Sun Fuquan, Fu Yuan, Zhu Wanqian, Xue Song. A study on multi-point gravity compensation of mirror bending system. Nucl Techn 2011;34(4):246–50.
[16] Wang Naxiu, Zhu Yi, Fu Yuan. Simulation of thermal distortion of DCM crystal indirectly cooled by LN2. High Energy Phys Nucl Phys 2006;30(8):802–5.
[17] Damkova J, Chvatal L, Jezek J, Oulehla J, Brzobohaty O, Zemanek P. Enhancement of the 'tractor-beam'pulling force on an optical bound structure. Light-Sci Appl 2018;7:17135.